

1 **Detectability of CO₂ flux signals by a space-based lidar mission**

2 Dorit M. Hammerling^a, S. Randolph Kawa^b, Kevin Schaefer^c, Scott Doney^d, and Anna M.
3 Michalak^e

4 ^a Institute for Mathematics Applied to Geosciences, National Center for Atmospheric
5 Research, Boulder, CO, USA

6 ^b NASA Goddard Space Flight Center, Greenbelt, MD, USA

7 ^c National Snow and Ice Data Center, Cooperative Institute for Research in Environmental
8 Sciences, University of Colorado at Boulder, USA

9 ^d Department of Marine Chemistry and Geochemistry, Woods Hole Oceanographic
10 Institution, Woods Hole, MA, USA

11 ^e Department of Global Ecology, Carnegie Institution for Science, Stanford, CA, USA

12

13

14 **Abstract**

15 Satellite observations of carbon dioxide (CO₂) offer novel and distinctive opportunities for
16 improving our quantitative understanding of the carbon cycle. Prospective observations include
17 those from space-based lidar such as the Active Sensing of CO₂ Emissions over Nights, Days,
18 and Seasons (ASCENDS) mission. Here we explore the ability of such a mission to detect
19 regional changes in CO₂ fluxes. We investigate these using three prototypical case studies,
20 namely the thawing of permafrost in the Northern High Latitudes, the shifting of fossil fuel
21 emissions from Europe to China, and changes in the source/sink characteristics of the Southern
22 Ocean. These three scenarios were used to design signal detection studies to investigate the
23 ability to detect the unfolding of these scenarios compared to a baseline scenario. Results
24 indicate that the ASCENDS mission could detect the types of signals investigated in this study,
25 with the caveat that the study is based on some simplifying assumptions. The permafrost thawing
26 flux perturbation is readily detectable at a high level of significance. The fossil fuel emission
27 detectability is directly related to the strength of the signal and the level of measurement noise.
28 For a nominal (lower) fossil fuel emission signal, only the idealized noise-free instrument test
29 case produces a clearly detectable signal, while experiments with more realistic noise levels
30 capture the signal only in the higher (exaggerated) signal case. For the Southern Ocean scenario,
31 differences due to the natural variability in the ENSO climatic mode are primarily detectable as a
32 zonal increase.

33 **1 Introduction**

34 Satellite observations of carbon dioxide (CO₂) offer novel and distinctive opportunities for
35 improving our quantitative understanding of the carbon cycle, which is an important scientific
36 and societal challenge with anthropogenic CO₂ emissions still on the rise. Prospective new
37 observations include those from space-based lidar such as the Active Sensing of CO₂ Emissions
38 over Nights, Days, and Seasons (ASCENDS) mission, which is proposed in "Earth Science and
39 Applications from Space: National Imperatives for the Next Decade" [*National Research
40 Council*, 2007] (henceforth referred to as the decadal survey). Notable features of this mission
41 include its ability to sample at night and at high latitudes. These conditions are prohibitive to
42 passive missions, such as the Greenhouse gases Observing SATellite (GOSAT) [e.g. *Kuze et al.*,
43 2009; *Yokota et al.*, 2009] and the Orbiting Carbon Observatory-2 (OCO-2) missions [e.g. *Crisp
44 et al.* 2004], due to their reliance on reflected sunlight. The lidar measurement technique
45 proposed for the ASCENDS mission further enables observing through some clouds and aerosols
46 [*Ehret et al.*, 2008], which also represent impediments and potential sources of bias for passive
47 missions [e.g., *Mao and Kawa*, 2004]. Extensive instrument design research and development is
48 ongoing, and proof of concept and validation studies indicate that ASCENDS will be able to
49 provide high-precision, unbiased observations with improved spatial coverage compared to
50 passive missions [e.g. *Spiers et al.*, 2011; *Abshire et al.*, 2010; *Kawa et al.*, 2010].

51 The primary goals of the ASCENDS mission are to address open questions in carbon cycle
52 science that focus on the identification of changing source/sink characteristics that are difficult to
53 observe using other current or anticipated observations. These goals were first articulated in the
54 decadal survey [*National Research Council*, 2007] and later refined in an ASCENDS mission
55 NASA Science Definition and Planning Workshop [*ASCENDS Workshop Steering Committee*,

56 2008]. They include detecting changes in the northern high latitude sources and sinks, detecting
57 changes in Southern Ocean source/sink characteristics, constraining anthropogenic CO₂
58 emissions, and increasing our understanding of biospheric carbon dynamics by differentiating
59 photosynthetic and respiration fluxes [ASCENDS Workshop Steering Committee, 2008]. CO₂
60 fluxes in the northern high latitudes and in the Southern Ocean may change substantially as
61 climate evolves, for example, and it is crucial to detect and attribute such changes quickly as they
62 could lead to large increases in atmospheric CO₂ concentrations and subsequent shifts in climate
63 dynamics [e.g. *Canadell et al.*, 2010].

64 Guided by these stated goals, this study explores the extent to which a space-based lidar
65 mission, using the ASCENDS mission concept as a guideline, can indeed contribute to these
66 pertinent carbon cycle science questions. We specifically focus on the ability of such a mission
67 to detect regional changes in fossil fuel emissions, high latitude CO₂ fluxes, and CO₂ fluxes in
68 the Southern Ocean. We investigate these using three prototypical case studies, namely the
69 thawing of permafrost in the Northern High Latitudes, the shifting of fossil fuel emissions from
70 Europe to the Peoples Republic of China (China), and changes in the source/sink characteristics
71 of the Southern Ocean related to the El Nino Southern Oscillation (ENSO). Realistic flux
72 scenarios are defined for each of these prototypical case studies, within the anticipated time
73 frame of the ASCENDS mission (i.e., the early to mid-2020s). These flux scenarios, combined
74 with a common set of baseline fluxes, form the basis of the presented analysis.

75 One can view the experimental setup as a hypothesis testing setup to answer the question if,
76 and how, the CO₂ concentration fields resulting from the baseline and perturbation fluxes, as
77 observed by an ASCENDS-like mission, are distinguishable. To that end, the three scenarios
78 described above are used in Observing System Simulations Experiments (OSSEs) to investigate

79 whether an ASCENDS-like mission will have the ability to identify the changes in atmospheric
80 CO₂ distributions associated with the changes in fluxes represented in each scenario. We apply
81 the geostatistical mapping approach developed in *Hammerling et al.* [2012a,b] to generate global
82 CO₂ maps based on ASCENDS-like sampling of the atmospheric CO₂ distribution resulting from
83 each flux scenario, and characterize the time required to observe statistically significant changes
84 in the inferred global CO₂ distribution, given varying assumptions about measurement
85 uncertainty.

86 **2 Model-Simulated Data**

87 The study is based on simulated data described below. The study period represents a full
88 year of the expected ASCENDS mission data.

89 **2.1 Baseline CO₂ Atmosphere**

90 We use the parameterized chemistry and transport model (PCTM) to produce a simulated
91 distribution of atmospheric CO₂ variability in space and time [*Kawa et al.*, 2004], based on the
92 baseline and perturbation scenarios. Model transport is driven by real-time analyzed
93 meteorology from the GEOS-5 Modern-Era Retrospective Analysis for Research and
94 Applications (MERRA) [*Rienecker et al.*, 2011] for 2007. CO₂ surface fluxes for the baseline
95 run include terrestrial vegetation physiological processes and biomass burning from CASA-
96 GFED3 [*Randerson et al.*, 1996; *van der Werf et al.*, 2010], seasonally-varying climatological
97 ocean fluxes from *Takahashi et al.* [2002], and fossil fuel burning from the CDIAC database
98 [*Andres et al.*, 2009]. CASA fluxes are driven by MERRA data, which results in
99 meteorologically-driven correspondence in the synoptic variability in the surface fluxes and
100 atmospheric transport. The monthly CASA fluxes are downscaled to 3-hourly fluxes in the

101 method of Olsen and Randerson [2004] as described by e.g. Chatterjee et al. [2012] and Shiga et
102 al. [2013]. The annual integral for the CASA fluxes is 1.53 Pg/yr representing a net source
103 largely due to high respiration in 2007. The average yearly CASA flux for the period 1997 to
104 2012 is 0.133 Pg/yr. The CASA fluxes used in this study are available at the North American
105 Carbon Data archive (<http://nacp-files.nacarbon.org/nacp-kawa-01/>). PCTM CO₂ output has
106 been extensively compared to in situ and remote sensing observations at a wide variety of sites,
107 and in most cases the model simulates diurnal to synoptic to seasonal variability with a high
108 degree of fidelity [e.g. *Law et al.*, 2008a; *Parazoo et al.*, 2008; *Bian et al.*, 2006; *Kawa et al.*,
109 2004]. For the simulations here, the model is run on a 1° × 1.25° latitude/longitude grid with 56
110 vertical levels and hourly output. We use 2007 meteorological, cloud and aerosol, and
111 reflectivity data for all components employed in the derivation of the simulated ASCENDS CO₂
112 observations.

113 **2.2 Perturbation flux scenarios**

114 Three case studies are developed based on areas of interest within carbon cycle science that
115 are directly relevant to the ASCENDS mission goals, namely the detection of regional changes in
116 fossil fuel emissions, high latitude CO₂ fluxes, and changes in CO₂ fluxes in the Southern Ocean.
117 They represent quantitatively plausible scenarios of changes in carbon fluxes, henceforth referred
118 to as perturbation flux scenarios, that could occur by the early to mid-2020s, the planned launch
119 timeframe for ASCENDS. These scenarios are used as prototypical examples of flux patterns
120 that give rise to the types of signals the ASCENDS mission endeavors to detect. The
121 perturbation fluxes are added to the baseline fluxes within the PCTM modeling framework
122 described in section 2.1 to produce the perturbation CO₂ atmospheres henceforth referred to as
123 perturbation runs.

124 **2.2.1 Permafrost carbon release**

125 The permafrost carbon feedback is an amplification of surface warming due to the release of
126 CO₂ and methane from thawing permafrost [Zimov *et al.* 2006]. Permafrost soils in the high
127 northern latitudes contain approximately 1700 Gt of carbon in the form of frozen organic matter
128 [Tarnocai *et al.* 2009]. Permafrost is perennially frozen ground remaining at or below 0°C for at
129 least two consecutive years [Brown *et al.* 1998] occupying about 24% of the exposed land area in
130 the Northern Hemisphere [Zhang *et al.* 1999]. As temperatures increase in the future and the
131 permafrost thaws, the organic material will also thaw and begin to decay, releasing CO₂ and
132 methane into the atmosphere. CO₂ and methane emissions from thawing permafrost will amplify
133 the warming due to anthropogenic greenhouse gas emissions [Zimov *et al.* 2006].

134 The permafrost carbon emissions scenario applied here uses projections of CO₂ fluxes from
135 thawing permafrost from Schaefer *et al.* [2011]. Schaefer *et al.* [2011] use the Simple
136 Biosphere/Carnegie-Ames-Stanford Approach (SiBCASA) land surface model [Schaefer *et al.*,
137 2008] driven by output from several General Circulation Models for the A1B scenario from the
138 IPCC Fourth Assessment report [Lemke *et al.*, 2007]. The fluxes are an ensemble mean of 18
139 projections from 2002 through 2200. We ran the PCTM model with the extracted fluxes for 2020
140 to 2022 and used the 2022 fluxes as perturbation fluxes. The annual integrals for the permafrost
141 perturbation fluxes are 0.613 PgC/yr, 0.641 PgC/yr and 0.752 PgC/yr for 2020 to 2022,
142 respectively.

143 The flux perturbations are concentrated in areas of discontinuous permafrost along the
144 southern margins of permafrost regions (Figure 1). In discontinuous permafrost regions, north-
145 facing slopes might form permafrost, while south-facing slopes may not. Permafrost
146 temperatures hover just below freezing, making these regions vulnerable to thaw for small

147 increases in atmospheric temperature. Normally, the surface soils in the active layer thaw each
148 summer and refreeze each winter. However, as temperatures increase, the thaw depth becomes
149 too deep to refreeze in the winter, forming a talik or layer of unfrozen ground above the
150 permafrost. The talik allows microbial decay to continue during winter when the surface soils
151 are frozen, resulting in year-round fluxes that peak in summer when soil temperatures are highest
152 (see Figure A1 in supplementary material).

153 The CO₂ concentrations of the baseline run were mean-adjusted to match the annual mean
154 of the perturbation run by applying a multiplicative adjustment. This adjustment preserves the
155 spatial patterns of the baseline run, while the global difference in concentrations between the
156 baseline and perturbation run is zero, so effectively a global flux-neutral scenario. This has been
157 done to focus this study on the detectability of changes in spatial patterns rather than detecting
158 the mean interannual increase in CO₂ concentrations that results from the strictly positive
159 perturbation fluxes over the two years of model spin-up and the investigated year.

160 **2.2.2 *Shift in fossil fuel emissions***

161 The fossil fuel flux perturbation scenario consists of a shift of fossil fuel emissions from
162 Europe to China; a shift that is in directional agreement with recent trends in these regions.
163 Fossil fuel emissions from China have increased rapidly over the last decades and China is now
164 largest emitter of CO₂ worldwide [Olivier *et al.*, 2012; Peters *et al.*, 2011]. By comparison,
165 fossil fuel emissions from Europe decreased 3% in 2011 relative to 2010 with an overall decline
166 over the last two decades [Olivier *et al.*, 2012]. We used two magnitudes of emission shift, from
167 here on referred to as the “lower” and “higher” signal, representing two points on a continuum of
168 possible emission changes around the year 2022.

169 The lower signal represents a 20% decrease of European emissions, with a 12% increase in
170 China (Figure 2) that exactly offsets the European decrease. The higher signal includes a 50%
171 decrease of emissions in Europe with a corresponding 30% increase in China (Figure 2), and is
172 used for illustration purposes only, as a decrease of this size is not expected in Europe within a
173 decade. All the percentage changes are in reference to 2007 emission levels, based on the v2011
174 2007 fossil fuel emissions from the CDIAC data base [Andres *et al.*, 2011]. The annual flux
175 integrals for the lower and higher signals are 0.228 PgC/yr and 0.571 PgC/yr, respectively. We
176 use these two shift settings as examples to draw broader conclusions on the detectability of these
177 types of signals as characterized by their the spatial and temporal patterns and their magnitudes.

178 The flux perturbations are globally flux neutral, in that European fossil fuel fluxes are
179 reduced by a set percentage in each month and the total emissions from China are increased by
180 the same mass amount. The decrease and increase is conducted proportionally to the existing
181 spatial pattern of the fluxes for each month, thereby preserving the spatial and temporal patterns
182 within the European and Chinese fluxes (Figures A2 and A3 in supplementary material). The
183 fluxes vary relatively little from month to month, on average +/- 15%. Overall, the signal to be
184 detected is a difference in the spatial distribution of CO₂ concentrations, with the global mean
185 remaining unchanged.

186 2.2.3 *Changes in Southern Ocean fluxes*

187 The Southern Ocean is of special interest to carbon cycle science, because its CO₂ fluxes are
188 highly uncertain [Gruber *et al.*, 2009], it is a region with apparent high sensitivity to climate
189 change [Le Quéré *et al.*, 2009], and this sensitivity has implications for the region's future as a
190 carbon sink because half of the ocean uptake of anthropogenic CO₂ is estimated to occur there
191 [e.g. Le Quéré *et al.*, 2009; Meredith *et al.*, 2012]. There is disagreement on the current and

192 future trend of the carbon flux in the Southern Ocean [*Le Quéré et al.*, 2009; *Law et al.*, 2008b].
193 The Southern Ocean is also a very sparsely sampled region, where the ability of the ASCENDS
194 mission to observe at high latitudes could provide valuable insights.

195 Variations in climate modes are a key driver of interannual variability in ocean carbon
196 exchange [e.g. *Field et al.*, 2007]. Here we evaluate the extent to which interannual variability
197 due to variations in climatic modes, such as the El Nino Southern Oscillation (ENSO), can be
198 detected as a reference for addressing potential changes in the sink/source characteristics of the
199 Southern Ocean using satellite observations. In other words, we use ENSO-related variability as
200 a prototypical example of the scale of variability to detect. To that end, the years 1977 and 1979
201 were chosen as examples of estimated flux patterns, as they represent large differences in ocean
202 fluxes due to variations in climatic modes.

203 The Southern ocean fluxes for this scenario are based on a hind cast simulation of the
204 Community Climate System Model (CCSM) Ocean Biogeochemical Elemental Cycle model as
205 described by Doney et al. [2009]. The fluxes were obtained at $1^{\circ} \times 1^{\circ}$ spatial and monthly
206 temporal resolution. The monthly difference between the Southern ocean flux anomaly for 1977
207 and 1979 is used as the perturbation flux for this scenario. Figure 3a and 3c show the average
208 flux perturbation for April through June and the full year, respectively. A year-round time series
209 of these monthly perturbation fluxes is shown in Figure A4 (supplementary material). The
210 magnitude of the perturbation fluxes (1977: 0.186 PgC/yr, 1979: -0.176 PgC/yr) is low relative
211 to the other two case studies. In contrast to the other two experiments, the sign of the
212 perturbation flux also varies by month and spatially within the region.

213 **2.3 Simulated ASCENDS CO₂ observations**

214 Anticipated ASCENDS sampling and random measurement error characteristics are derived
215 from model output and observations in a method similar to that of Kawa et al. [2010] and Kiemle
216 et al. [2014]. The Cloud-Aerosol Lidar and Infrared Pathfinder Satellite Observation (CALIPSO)
217 orbital track is used to simulate the expected ASCENDS sampling. Synthetic observations are
218 sampled from model output at the nearest time to the satellite over-flight, and interpolated in
219 space to the CALIPSO sample locations. A vertical weighting function, appropriate to an
220 ASCENDS laser instrument operating at a wavelength near 1.57 um, is applied to the model
221 pseudo-data profile to produce column average mixing ratio values [Ehret et al., 2008]. We
222 consider only random errors due to photon counting. Potential bias errors [e.g. Baker et al.,
223 2010], which could significantly complicate the analysis if correlated with geophysical variables
224 of interest (e.g., land/ocean or vegetation cover), are not included.

225 CALIPSO measurements of total cloud and aerosol optical depth (OD) are used to calculate
226 the ASCENDS laser attenuation. CALIPSO OD data are reported every 5 km (corresponding to
227 every 0.7435 s) along track and this forms the basic ASCENDS sample set. Surface lidar
228 backscatter (β), also needed for error estimation, follows from MODIS measured spectral
229 reflectance over land and the glint formulation of Hu et al. [2008] over water using daily
230 MERRA 10-m wind speeds. Surface reflectivity over land is interpolated from MODIS (Terra +
231 Aqua) 5-km 16-day composite nadir BRDF-adjusted reflectance data (α) at 1.64 μ m (band 6),
232 which are available every 8 days [Schaaf et al., 2002]. Land reflectance is scaled by a factor of
233 1.23 to account for the land ‘hot spot’ backscatter effect [Disney et al., 2009], i.e., β (sr^{-1}) = 1.23
234 α/π . Backscatter values of 0.08 sr^{-1} and 0.01 sr^{-1} are used to fill missing areas of MODIS data

235 over land and over snow/ice, respectively, where ice and snow cover is determined from
236 MERRA data.

237 In order to make our study method applicable for a range of possible CO₂ laser sounder
238 instrument implementations, we scale the errors globally to a nominal error value for clear-air
239 conditions at Railroad Valley, NV ($\beta = 0.176$, $T = 1$) and a 10-s (67.2 km) sample integration.
240 Thus, a given instrument model can be characterized by its random error at the Railroad Valley
241 reference point and the global distribution of errors estimated from OD and β . The individual
242 sounding errors at the 5 km CALIPSO resolution are calculated using:

$$\sigma_{5\text{km}} = \frac{3.667 * \sigma_{\text{ref}}}{\left(\frac{\beta * T^2 * \text{sdf}}{0.176}\right)^{0.5}}, \quad (1)$$

243 where σ_{ref} is the 10-s reference instrument random error (standard deviation) at Rail Road
244 Valley, T the transmittance, sdf the surface detection frequency, and 0.176 is the Rail Road
245 Valley backscatter reference value at 1.57 μm , which corresponds to one of the potential
246 ASCENDS instrument designs [Abshire *et al.*, 2010]. The transmittance is calculated from the
247 CALIPSO (*OD*) using $T = e^{-OD}$.

248 Soundings with an optical depth greater than 0.3 or where the surface detection frequency
249 equals zero are filtered out and considered 'not retrieved'. The surface detection frequency
250 equals zero when none of the 1-km averaged CALIPSO samples in a 5-km average can see a
251 ground return, i.e., the clouds/aerosol were too thick to get a return from the ground. For this
252 study we a 10-s along-track average as our pseudo-data measurement granule [Kawa *et al.*,
253 2010]. Using this setup, the maximum number of soundings constituting one observation is 14.
254 The 10-s observation error variances are then calculated by averaging the 5-km error variances

255 within each 10-s time interval and dividing this average by the number of retrieved soundings.
256 This setup implies the assumption that retrieval errors between individual soundings are spatially
257 and temporally uncorrelated. We include three measurement noise settings in the study. A no-
258 measurement noise setting for reference purposes, and medium and high noise settings, which
259 use Rail Road Valley 10-s reference instrument random errors (σ_{ref}) of 0.5 and 1 ppm,
260 respectively. Once the measurement error variance has been determined for each location
261 following the procedure described above, a random sample from a normal distribution with that
262 variance is drawn and added to the PCTM model CO₂ value to define a pseudo-data observation.
263 The global mean errors (σ_{obs}) are 2.1 and 4.2 ppm, respectively, for the medium and high noise
264 settings. Figure 4b provides an example of four days of global observations. Different random
265 seed numbers are used for the errors in the baseline and the perturbation runs.

266 **3 Methods**

267 **3.1 Mapping approach**

268 We use a geostatistical mapping approach [*Hammerling et al.*, 2012a,b] to create contiguous
269 interpolated maps, i.e. global mapped ("Level 3") products, for the comparison. Satellite CO₂
270 observations contain large gaps and high measurement errors such that meaningful spatially-
271 comprehensive comparisons at synoptic timescales are often precluded using the observations
272 directly. Using gap-filled products makes it possible to conduct synoptic, global comparisons.
273 The approach presented in *Hammerling et al.* [2012a,b] also yields spatially-explicit
274 uncertainties (eq. 7 in Hammerling et al. [2012a]) of the mapped products. These may be lower
275 than the uncertainties of the individual observations in areas where the correlation with nearby
276 observations can be leveraged, which in turn can facilitate signal detection.

277 The applied mapping methodology yields global mapped CO₂ concentrations with
278 uncertainty measures without invoking assumptions about fluxes or atmospheric transport. The
279 method leverages the spatial correlation in the atmospheric CO₂ concentration field,
280 parameterized as an exponential covariance function with spatially-varying variance and
281 correlation range parameters using a moving-window circular domain of 2000 km. These
282 parameters are estimated from the observations, and thus not imposed *a priori*. Methodological
283 details are given in *Hammerling et al.* [2012a,b].

284 Specific to this study, we filter the pseudo-data observations to those with a measurement
285 error standard deviation below a certain threshold. This is analogous to imposing a quality
286 criterion when delivering remote sensing data instead of making all retrievals available. For the
287 medium (high) measurement error setup this threshold is 1.5 (3.0) ppm. This choice represents a
288 balance between spatial coverage and robustness of the covariance estimation procedure and was
289 determined in a sensitivity analysis (results not shown). For the "no error" setup, which is only
290 used as a theoretical best case, we use observations at the same locations as for the medium and
291 high measurement setups, but without any noise added. We include this case to isolate any
292 potential limitations of the methodology and the spatial coverage from those related to the
293 instrument capabilities.

294 Mapping CO₂ satellite observations at synoptic time scales makes it possible to capture the
295 dynamic behavior of CO₂ in the atmosphere [*Hammerling et al.*, 2012a, b]. Based on
296 preliminary studies evaluating mapping performance for different time periods, 4-day periods
297 were found to provide the best balance between ensuring good data coverage while also
298 capturing synoptic behavior for ASCENDS-like observations. Figure 4 shows an example of a
299 4-day (August 1- 4 2007) period. The average modeled CO₂ distribution is shown for reference,

300 and only the observations are used in the subsequent mapping procedure. Each 4-day period is
301 mapped independently from other 4-day periods and for the baseline and perturbation runs. For
302 January, only six 4-day periods were mapped due to missing CALIPSO data; for all other
303 months, seven 4-day periods were mapped for a total of 83 4-day maps for each of the baseline
304 and perturbation cases. These mapped fields were then used as input data in the subsequent
305 comparison analysis described in Section 3.2

306 **3.2 Comparison approach**

307 The detectability of a signal is assessed point-wise for each model grid cell by comparing
308 the mapped concentrations from the baseline run and the perturbation run, and determining
309 whether the observed differences exceed their associated uncertainties. The uncertainty of the
310 difference between two mapped concentration fields, expressed as a variance, is the sum of the
311 estimation variances of the baseline, $\sigma_{\hat{y}_{base}}^2$, and the perturbation, $\sigma_{\hat{y}_{per}}^2$, mapped products:

$$\sigma_{diff}^2 = \sigma_{\hat{y}_{base}}^2 + \sigma_{\hat{y}_{per}}^2$$

312 For ease of interpretation and visualization purposes, the comparison results are binned by their
313 relative uncertainties, where the absolute value of the difference exceeds one, two or three
314 standard deviations, respectively, of the uncertainty of the difference.

315 Due to the measurement error added to the observations, together with the sparseness of the
316 available observations, individual 4-day maps do not exhibit detectable differences in a statistical
317 sense, and the question then becomes to identify a time period over which such 4-day maps must
318 be averaged before a significant signal emerges. Under the assumption of temporal
319 independence, the uncertainty (expressed as a variance) of the temporal mean is the mean

320 mapping variance of the individual periods divided by the number of periods. The assumption of
321 temporal independence was evaluated by conducting temporal variogram analyses for sets of
322 mapping errors at randomly selected locations (results not shown), and no compelling indication
323 to contradict this assumption was found.

324 **4 Results and Discussion**

325 On a high level, one can view the query of detecting atmospheric CO₂ concentration signals
326 resulting from flux perturbations as two distinct, if connected, questions. The first question is
327 how characteristics of the flux perturbations are translated to, and preserved in, the atmospheric
328 CO₂ concentrations, i.e. what is the signature (or signal) of a set of flux perturbations of interest
329 in the atmospheric CO₂ concentrations. The second question is how well a given observing
330 system, in our case the ASCENDS mission, can capture the presence of this signal. Both of
331 these aspects are discussed in the following sections, which are organized by the three
332 investigated scenarios.

333 **4.1 Detectability of permafrost carbon release**

334 A significant signal can be detected in the case of the anticipated permafrost carbon
335 emissions (Figures 5 and A5). The challenge is in capturing longitudinal and latitudinal
336 gradients, which can better attribute the increase to the permafrost region, as opposed to just
337 detecting a zonal increase. While signal detection is not directly targeted at quantifying carbon
338 fluxes, insights on the detectability of spatial gradients are highly relevant for studies targeting
339 flux detections, e.g. atmospheric inverse modeling studies. With this in mind, a judicious choice
340 of the temporal aggregation periods over which the comparisons are conducted is important.

341 Because of the seasonality of the fluxes in the permafrost carbon release scenario (Figure
342 A1), the gradients in the atmospheric CO₂ distribution are most evident in the months following
343 the start of the spring thaw. As a result, averaging over spring/summer months yields a clearer
344 identification of the geographic origin of the signal relative to aggregating maps over the full
345 year. While the concentration signal is highest around September (Figure A1), or even later in
346 the year, when the active layer is deepest, the concentration signals indicative of the spatial
347 pattern of the tundra fluxes are most distinct in the late spring/early summer months before the
348 effects of atmospheric mixing take over. By August, atmospheric mixing, which occurs rapidly
349 in the Arctic, causes the spatial signature of the tundra melting fluxes to be replaced by the
350 dominant signal of a zonal increase. Some further evidence of this phenomenon can be observed
351 by comparing Figures 1b and 1d: the 3-month signal retains more of the spatial characteristics,
352 whereas the yearly signal represents a zonal increase where the elevated concentrations have
353 spread towards the pole. This phenomenon is caused by the specific combination of the temporal
354 pattern of the permafrost carbon release and rapid atmospheric mixing in the High Northern
355 Latitudes.

356 Figures 5 and A5 show a summary of the detection results for the permafrost carbon release
357 scenario. While the 3-months results feature comparatively more noise, the recognition of the
358 spatial pattern in the significance plots is also improved. Even for the high noise scenario, the
359 land origin of the signal is better seen in the 3-month maps relative to the yearly plots. The
360 results for the different noise levels are as expected; lower noise provides a more accurate
361 mapped concentration field (Figure A5). Overall, the permafrost CO₂ perturbation is detectable
362 for both levels of measurement noise considered, and spatial gradients are best detected using
363 two to three month aggregation periods in the late spring/early summer.

364 **4.2 Detectability of shift in fossil fuel emissions**

365 The examined fossil fuel emissions perturbations lead to a pronounced spatial signature that
366 is localized over Europe and China (Figures 2c, g; 2d, h; A2; A3). This is in contrast to the other
367 two experiments (see Figures 1d and 3d), where the detailed spatial signatures are largely lost
368 and especially the yearly signals represent primarily zonal increases. In addition, the magnitude
369 of the lower fossil fuel perturbation signal is very low, which, combined with its small spatial
370 extent, renders the weak fossil fuel signal the most difficult to detect among the investigated
371 scenarios. This exemplifies the challenge of detecting small and localized flux changes from
372 satellite observations.

373 The highly localized nature of the signal over Europe and China suggests that changes in
374 fluxes would be detectable and attributable to a given region, even if these fluxes were not offset
375 by a corresponding shift in emissions within a similar latitudinal range. It is interesting to
376 observe the different dispersion patterns of the European and Chinese emissions, especially when
377 considering their latitudinal range. The effect on the atmospheric concentrations of the European
378 emissions can be observed from equatorial Africa to the Arctic, whereas the range of the Chinese
379 emissions is more limited to their originating latitudinal band (see Figure 2h).

380 Given the relative lack of seasonality in the fossil fuel perturbation scenarios, averaging
381 over longer periods of time leads to better detectability (Figure 6). Although atmospheric
382 transport clearly plays a role, the atmospheric signal remains indicative of the source region of
383 the perturbation flux throughout the seasons. Figure 6h, for example, shows evidence that both
384 the source and downwind regions of the emissions have a significant signature in the
385 atmosphere.

386 The effect of varying measurement noise levels on the detectability is again as expected;
387 increasing measurement noise leads to decreased significance in the results and requires in turn
388 longer averaging periods. For the higher signal, all three noise levels capture the signal in the
389 yearly results, which is not the case for the lower signal, where only the no error case clearly
390 captures the signal (Figure A6). There is some evidence that a significant signal is detectable in
391 the yearly medium and high error measurement noise cases (Figure 6), and given the nature of
392 the signal discussed above, the signal is expected to appear more clearly when averaging over
393 periods exceeding one year. Overall, these findings imply that ASCENDS can in principle detect
394 anthropogenic signal components, but depending on the strength of the signal, detection might
395 require multiple years. It is hence feasible that ASCENDS can serve to validate anthropogenic
396 emission changes over the course of its mission, but is likely not ideal as the primary monitoring
397 tool for such flux changes.

398 **4.3 Detectability of changes in Southern Ocean fluxes**

399 The detection of changes in the Southern Ocean source/sink characteristics is challenging as
400 a result of a confluence of different factors. The overall magnitude of the signal in the Southern
401 Oceans is rather weak, with the absolute value of the signal never exceeding 0.4 ppm in the
402 column. In addition, this scenario involves sub-seasonal and sub-regional-scale flux variability
403 that is superimposed on a seasonal pattern in the fluxes (Figure A4). Atmospheric mixing also
404 plays a role insofar as it obscures the Southern Ocean as the origin of the signal, as was also
405 observed in the permafrost carbon release scenario. However, applying the remedy of using a
406 shorter averaging period before atmospheric mixing hides the origin of the signal is not as clear-
407 cut for the Southern Ocean scenario, because the overall signal is weaker. Spatial gradients
408 associated with the Southern Ocean flux perturbation are most evident in the spring and early

409 summer (Figure 3). Later in the year, although the concentration signal is stronger, the
410 concentration increase has spread pole-ward and is less attributable to the Southern Ocean.

411 For all measurement noise setups, the yearly results clearly indicate a zonal increase in the
412 High Southern Latitudes (Figures 7 and A8). However, it is less clear whether the pattern is
413 indicative of the Southern Ocean being the source region within the zonal band. The spatial
414 pattern of the 3-month results (Figures 7b) is more indicative of the Southern Ocean as the
415 source region, but the significance levels are not very high. The most beneficial approach for the
416 Southern Ocean scenario appears to be conducting analyses over periods of multiple lengths, and
417 drawing conclusions from the joint picture emerging from these analyses. In summary,
418 ASCENDS can detect a Southern Ocean signal representative of differences due to natural
419 variability in the ENSO climatic mode. ASCENDS may provide a unique measurement view of
420 these regions because the pervasive cloudiness and low sun angles present difficult conditions
421 for passive satellite CO₂ sensors. Due to the low magnitude and small-scale variability within
422 the fluxes giving rise to the signal, however, attributing the signal to specific ocean regions or
423 biogeophysical processes will likely require additional corroborative information.

424 **5 Conclusions**

425 This work assesses the degree to which ASCENDS, a planned lidar CO₂ observing satellite
426 mission, can contribute to the detection of three types of CO₂ flux change scenarios relevant to
427 global carbon cycle science: the release of carbon due to the thawing of permafrost in the
428 Northern High Latitudes, the shifting of fossil fuel emissions from Europe to China, and ENSO-
429 related changes in the source/sink characteristics in the Southern Ocean. These three scenarios
430 were used to design OSSEs for signal detection studies to investigate if the ASCENDS mission

431 has the ability to detect the unfolding of these scenarios compared to a baseline scenario. Two
432 different levels of measurement noise and a no measurement noise reference case were
433 investigated.

434 This study is based on a number of simplifications. For each scenario, the only flux
435 component that is varied is the flux component under investigation, while all other fluxes are
436 fixed. In reality, many changes might occur simultaneously and the resulting CO₂ concentration
437 signal patterns might overlap, which makes signal detection more challenging. We have
438 introduced some additional variability by sampling and mapping the baseline concentration field
439 rather than assuming a static baseline concentration field in the comparison procedure, however,
440 that might not be equivalent to, for example, having misspecified biospheric fluxes. Such
441 misspecifications could be aliased with the true signals and misleading signal patterns could
442 occur. This could impact the conclusions of this study insofar that it would be more difficult to
443 link detectable signals with the underlying change in fluxes.

444 The results indicate that the ASCENDS mission can in principle detect the types of signals
445 investigated in this study. The permafrost thawing flux perturbation is readily detectable at a
446 high level of significance. Spatial gradients, which are of great interest for process attribution,
447 were best detected using two or three month aggregation periods in the late spring/early summer.
448 For the Southern Ocean scenario, differences due to the natural variability in the ENSO climatic
449 mode were primarily detectable as a zonal increase. The relative magnitude of the signal,
450 however, is much smaller than the permafrost-thawing signal. Spatial and temporal high-
451 frequency changes in the anomaly fluxes produce additional variability in the signal, making
452 detection of more detailed gradients than a zonal increase challenging for the Southern Ocean

453 scenario. Conducting analyses over periods of varying lengths and analyzing them jointly
454 provides a possible diagnostic strategy.

455 The fossil fuel emission detectability is directly related to the strength of the signal and the
456 level of measurement noise. As is true for all scenarios, the effect of varying measurement noise
457 levels is as expected: increasing measurement noise levels lead to decreased significance in the
458 results and require in turn longer averaging periods. For the nominal (lower) fossil fuel emission
459 signal, only the noise-free instrument test produces a clearly detectable signal, while all three
460 noise levels capture the higher (exaggerated) signal case. The emergence of a detectable signal
461 suggests that averaging over periods longer than the one-year period considered in this study
462 would also render signals of the magnitude of the lower fossil fuel emission signal detectable.

463 All in all, the expected precision and sampling characteristics of ASCENDS promise to
464 substantially enhance our ability to detect variations in CO₂ fluxes and to inform the mechanisms
465 that control them. Future work includes comparing the signal detection performance of
466 ASCENDS to passive sensors, which might be employed within the time frame of the
467 ASCENDS mission. Additional future work entails a comprehensive study of the effect of
468 uncertainties in fluxes other than those defining the signal on the detectability of the signal, for
469 example, by using an ensemble of biospheric fluxes to vary the baseline fluxes.

470 **Acknowledgements**

471 This material is based upon work supported by the National Aeronautics and Space
472 Administration under Grant NNX08AJ92G issued through the Research Opportunities in Space
473 and Earth Sciences (ROSES) Carbon Cycle Science program and by Jet Propulsion Laboratory

474 subcontract 1442785 as well as the ASCENDS Science Requirements Definition Team. S.

475 Doney acknowledges support from U.S. National Science Foundation (AGS-1048827).

476 All the data used in this study can be requested by emailing Dorit Hammerling

477 (dorith@ucar.edu). We thank Robert Andres for providing CDIAC fossil fuel emission fluxes

478 and his advice in applying them. We thank Ivan Lima for support with the Southern Ocean

479 fluxes, and Michael Manyin and Yuping Liu for executing PCTM model runs.

480

481 **References**482 **REFERENCES**

483 Abshire, J. B., H. Riris, G. R. Allan, C. J. Weaver, J. Mao, X. Sun, W. E. Hasselbrack, S. R.
484 Kawa, and S. Biraud (2010), Pulsed airborne lidar measurements of atmospheric CO₂ column
485 absorption, *Tellus B*, 62(5), 770-783, doi: 10.1111/j.1600-0889.2010.00502.x.

486 Andres, R. J., T. A. Boden, and G. Marland (2009), Monthly Fossil-Fuel CO₂ Emissions: Mass
487 of Emissions Gridded by One Degree Latitude by One Degree Longitude, *Carbon Dioxide*
488 *Information Analysis Center, Environmental Sciences Division, Oak Ridge National Laboratory,*
489 *Oak Ridge, Tennessee 37831-6290, U. S. A.*

490 Andres, R. J., J. S. Gregg, L. Losey, G. Marland, and T. A. Boden (2011), Monthly, global
491 emissions of carbon dioxide from fossil fuel consumption, *Tellus B*, 63(3), 309-327, doi:
492 10.1111/j.1600-0889.2011.00530.x.

493 ASCENDS Workshop Steering Committee (2008), Active Sensing of CO₂ Emissions over
494 Nights, Days, and Seasons (ASCENDS) Mission NASA Science Definition and Planning
495 Workshop Report, 1-78.

496 Baker, D.F., H. Bösch, S.C. Doney, D. O'Brien, and D.S. Schimel, 2010: Carbon source/sink
497 information provided by column CO₂ measurements from the Orbiting Carbon Observatory,
498 *Atmosp. Chem. Physics*, 10, 4145-4165, doi:10.5194/acp-10-4145-2010.

499 Bian, H., S. R. Kawa, M. Chin, S. Pawson, Z. Zhu, P. Rasch, and S. Wu (2006), A test of
500 sensitivity to convective transport in a global atmospheric CO₂ simulation, *Tellus B*, 58(5), 463-
501 475, doi: 10.1111/j.1600-0889.2006.00212.x.

502 Canadell, J. G., C. L. Quéré, M. R. Raupach, C. B. Field, E. T. Buitenhuis, P. Ciais, T. J.
503 Conway, N. P. Gillett, R. A. Houghton, and G. Marland (2010), Carbon sciences for a new
504 world, *Current Opinion in Environmental Sustainability*, 2(209).

505 Chatterjee, A., A.M. Michalak, J.L. Anderson, K.L. Mueller, V. Yadav (2012) "Toward reliable
506 ensemble Kalman filter estimates of CO₂ fluxes", *Journal of Geophysical Research –*
507 *Atmospheres*, 117, D22306, doi:10.1029/2012JD018176.

508 Crisp, D., R. M. Atlas, F. Bréon, L. R. Brown, J. P. Burrows, P. Ciais, B. J. Connor, S. C.
509 Doney, I. Y. Fung, D. J. Jacob, C. E. Miller, D. M. O'Brien, S. Pawson, J. T. Randerson, P. J.
510 Rayner, R. J. Salawitch, S. P. Sander, B. Sen, G. L. Stephens, P. P. Tans, G. C. Toon, P. O.
511 Wennberg, S. C. Wofsy, Y. L. Yung, Z. Kuang, B. Chudasama, G. Sprague, B. Weiss, R.
512 Pollock, D. Kenyon, and S. Schroll (2004), The Orbiting Carbon Observatory (OCO) mission
513 *Advances in Space Research*, 34(4), 700-709, doi: 10.1016/j.asr.2003.08.062.

514 Disney, M. I., P. E. Lewis, M. Bouvet, A. Prieto-Blanco, and S. Hancock (2009), Quantifying
515 Surface Reflectivity for Spaceborne Lidar via Two Independent Methods, *Geoscience and*
516 *Remote Sensing, IEEE Transactions on*, 47(9), 3262-3271.

517 Doney, S. C., I. Lima, R. A. Feely, D. M. Glover, K. Lindsay, N. Mahowald, J. K. Moore, and R.
518 Wanninkhof (2009), Mechanisms governing interannual variability in upper-ocean inorganic
519 carbon system and air-sea CO₂ fluxes: Physical climate and atmospheric dust, *Deep Sea*
520 *Research Part II: Topical Studies in Oceanography*, 56(8–10), 640-655, doi:
521 10.1016/j.dsr2.2008.12.006.

522 Ehret, G., C. Kiemle, M. Wirth, A. Amediek, A. Fix, and S. Houweling (2008), Space-borne
523 remote sensing of CO₂, CH₄, and N₂O by integrated path differential absorption lidar: a
524 sensitivity analysis, *Applied Physics B: Lasers and Optics*, 90(3), 593-608, doi: 10.1007/s00340-
525 007-2892-3.

526 Field, C. B., J. Sarmiento, and B. Hales (2007), The carbon cycle of North America in a global
527 context., in *The First State of the Carbon Cycle Report (SOCCR): The North American Carbon*
528 *Budget and Implications for the Global Carbon Cycle. A Report by the U.S. Climate Change*
529 *Science Program and the Subcommittee on Global Change Research*, edited by A.W. King, L.
530 Dilling, G.P. Zimmerman, D.M. Fairman, R.A. Houghton, G. Marl, A.Z. Rose, and T.J.
531 Wilbanks, pp. 21-28, National Oceanic and Atmospheric Administration, National Climatic Data
532 Center, Asheville, NC.

533 Gruber, N. et al. (2009), Oceanic sources, sinks, and transport of atmospheric CO₂, *Global*
534 *Biogeochem. Cycles*, 23.

535 Hammerling, D. M., A. M. Michalak, and S. R. Kawa (2012a), Mapping of CO₂ at high
536 spatiotemporal resolution using satellite observations: Global distributions from OCO-2, *J.*
537 *Geophys. Res.*, 117, D06306, doi: 10.1029/2011JD017015.

538 Hammerling, D. M., A. M. Michalak, C. O'Dell, and S. R. Kawa (2012b), Global CO₂
539 distributions over land from the Greenhouse Gases Observing Satellite (GOSAT), *Geophys. Res.*
540 *Lett.*, 39(8), L08804, doi: 10.1029/2012GL051203.

541 Hu, Y. et al. (2008), Sea surface wind speed estimation from space-based lidar measurements,
542 *Atmospheric Chemistry and Physics*, 8(13), 3593-3601, doi: 10.5194/acp-8-3593-2008.

543 Kawa, S. R., D. J. Erickson III, S. Pawson, and Z. Zhu (2004), Global CO₂ transport simulations
544 using meteorological data from the NASA data assimilation system, *J. Geophys. Res.*, 109, doi:
545 10.1029/2004JD004554.

546 Kawa, S. R., J. Mao, J. B. Abshire, G. J. Collatz, X. Sun, and C. J. Weaver (2010), Simulation
547 studies for a space-based CO₂ lidar mission, *Tellus B*, 62(5), 759-769, doi: 10.1111/j.1600-
548 0889.2010.00486.x.

549 Kiemle, C., S. R. Kawa, M. Quatrevaelet, and E. V. Browell (2014), Performance simulations for
550 a spaceborne methane lidar mission, *J. Geophys. Res. Atmos.*, 119, doi:10.1002/2013JD021253.

551 Kuze, A., H. Suto, M. Nakajima, and T. Hamazaki (2009), Thermal and near infrared sensor for
552 carbon observation Fourier-transform spectrometer on the Greenhouse Gases Observing Satellite
553 for greenhouse gases monitoring, *Appl. Opt.*, 48, 6716-6733, doi:10.1364/AO.48.006716.

554 Law, R. M. et al. (2008a), TransCom model simulations of hourly atmospheric CO₂:
555 Experimental overview and diurnal cycle results for 2002, *Global Biogeochem. Cycles*, 22(3),
556 GB3009, doi: 10.1029/2007GB003050.

557 Law, R. M., R. J. Matear, and R. J. Francey (2008b), Comment on Saturation of the Southern
558 Ocean CO₂ Sink Due to Recent Climate Change, *Science*, 319(5863), 570.

559 Le Quéré, C., M. R. Raupach, J. G. Canadell, and E. A. Marland (2009), Trends in the sources
560 and sinks of carbon dioxide, *Nature Geosci.*, 2(12), 831-836.

561 Lemke, P. et al. (2007), Changes in snow, ice and frozen ground, in *Climate Change 2007: The
562 Physical Science Basis: Contribution of Working Group I to the Fourth Assessment Report of the
563 Intergovernmental Panel on Climate Change*, edited by S. Solomon, D. Qin, M. Manning, Z.
564 Chen, M. Marquis, KB Averyt, M. Tignor, and HL Miller, Cambridge Univ. Press, Cambridge,
565 UK.

566 Mao, J. and S. R. Kawa (2004), Sensitivity Studies for Space-Based Measurement of
567 Atmospheric Total Column Carbon Dioxide by Reflected Sunlight, *Appl. Opt.*, 43(4), 914-927.

568 Meredith, M. P., A. C. N. Garabato, A. M. Hogg, and R. Farneti (2012), Sensitivity of the
569 Overturning Circulation in the Southern Ocean to Decadal Changes in Wind Forcing, *J. Climate*,
570 25(1), 99-110.

571 National Research Council (Ed.) (2007), *Earth Science and Applications from Space: National
572 Imperatives for the Next Decade and Beyond*, 456 pp., The National Academies Press,
573 Washington, DC 20001.

574 Olivier, J., G. Janssens-Maenhout, and J. Peters (2012), *Trends in Global CO₂ Emissions; 2012
575 Report*, PBL Netherlands Environmental Assessment Agency; Ispra: Joint Research Centre, The
576 Hague, Netherlands.

577 Olsen, S. C. and J. T. Randerson (2004), Differences between surface and column atmospheric
578 CO₂ and implications for carbon cycle research, *J. Geophys. Res.*, 109, D02301, doi:
579 10.1029/2003JD003968.

580 Parazoo, N. C., A. S. Denning, S. R. Kawa, K. D. Corbin, R. S. Lokupitiya, and I. T. Baker
581 (2008), Mechanisms for synoptic variations of atmospheric CO₂ in North America, South
582 America and Europe, *Atmospheric Chemistry and Physics*, 8(23), 7239-7254.

583 Peters, G. P., G. M. G, C. L. Quéré, T. Boden, J. G. Canadell, and M. R. Raupach (2011), Rapid
584 growth in CO₂ emissions after the 2008-2009 global financial crisis, *Nature Climate Change*, 2,
585 2-4.

586 Randerson, J. T., M. V. Thompson, C. M. Malmstrom, C. B. Field, and I. Y. Fung (1996),
587 Substrate limitations for heterotrophs: Implications for models that estimate the seasonal cycle of
588 atmospheric CO₂, *Global Biogeochem. Cycles*, 10(4), 585-602, doi: 10.1029/96GB01981.

589 Rienecker, M. M. et al. (2011), MERRA: NASA's Modern-Era Retrospective Analysis for
590 Research and Applications, *J. Clim.*, 24(14), 3624-3648.

591 Schaaf, C. B. et al. (2002), First operational BRDF, albedo nadir reflectance products from
592 MODIS, *Remote Sens. Environ.*, 83(1–2), 135-148, doi: 10.1016/S0034-4257(02)00091-3.

593 Schaefer, K., T. Zhang, L. Bruhwiler, and A. P. Barrett (2011), Amount and timing of permafrost
594 carbon release in response to climate warming, *Tellus B*, 63(2), 165-180, doi: 10.1111/j.1600-
595 0889.2011.00527.x.

596 Schaefer, K., G. J. Collatz, P. Tans, A. S. Denning, I. Baker, J. Berry, L. Prihodko, N. Suits, and
597 A. Philpott (2008), Combined Simple Biosphere/Carnegie-Ames-Stanford Approach terrestrial
598 carbon cycle model, *J. Geophys. Res.*, 113, G03034, doi:10.1029/2007JG000603

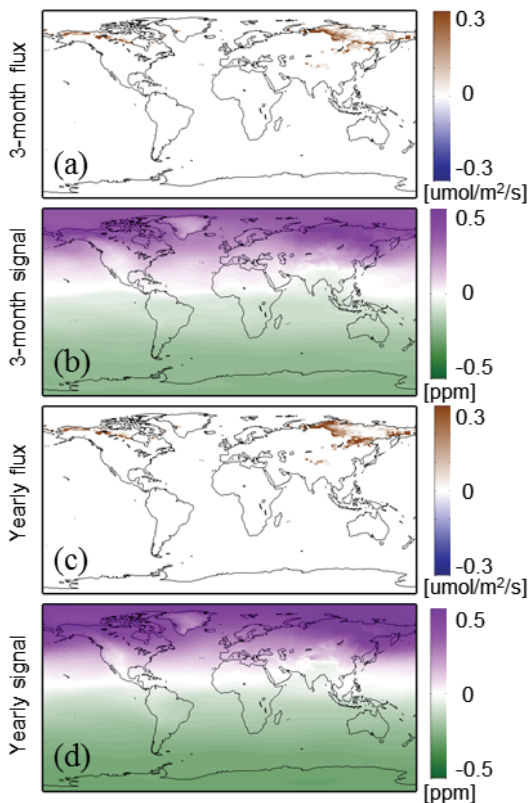
599 Shiga, Y.P., A.M. Michalak, S.R. Kawa, R.J. Engelen (2013) “In-situ CO₂ monitoring network
600 evaluation and design: A criterion based on atmospheric CO₂ variability”, *Journal of*
601 *Geophysical Research – Atmospheres*, 118, 2007-2018, doi: 10.1002/jgrd.50168.

602 Spiers, G. D., R. T. Menzies, J. Jacob, L. E. Christensen, M. W. Phillips, Y. Choi, and E. V.
603 Browell (2011), Atmospheric CO₂ measurements with a 2 μm airborne laser absorption
604 spectrometer employing coherent detection, *Appl. Opt.*, 50(14), 2098-2111, doi:
605 10.1364/AO.50.002098.

606 Takahashi, T. et al. (2002), Global sea–air CO₂ flux based on climatological surface ocean pCO₂,
607 and seasonal biological and temperature effects, *Deep Sea Research Part II: Topical Studies in*
608 *Oceanography*, 49(9–10), 1601-1622, doi: 10.1016/S0967-0645(02)00003-6.

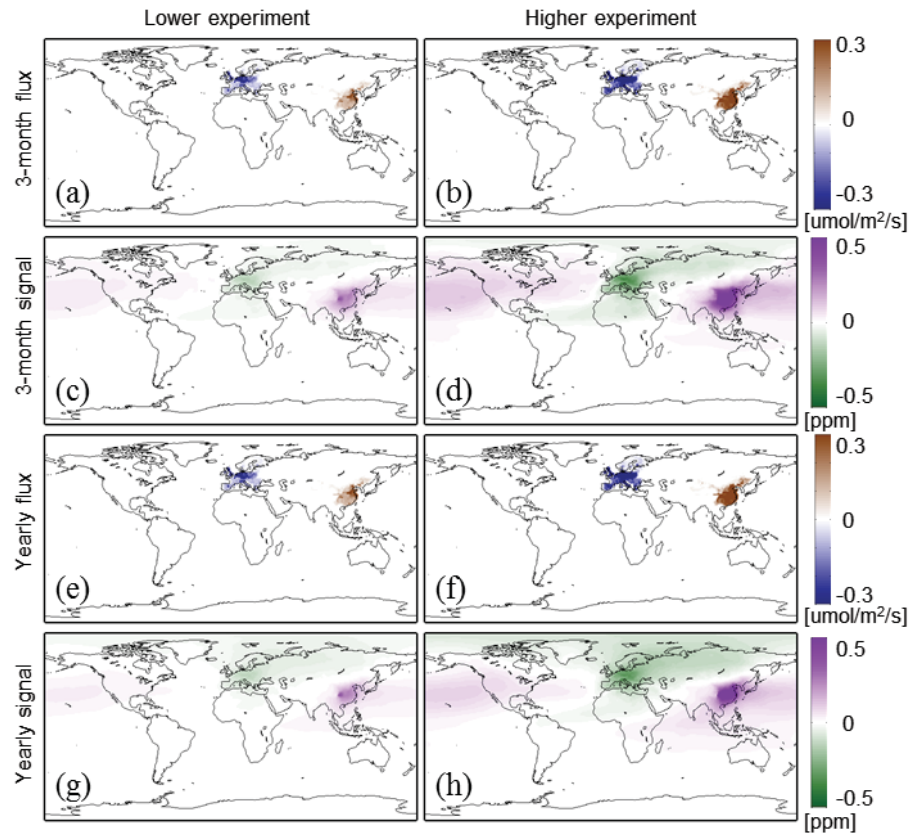
609 van der Werf, G. R., J. T. Randerson, L. Giglio, G. J. Collatz, M. Mu, P. S. Kasibhatla, D. C.
610 Morton, R. S. DeFries, Y. Jin, and T. T. van Leeuwen (2010), Global fire emissions and the
611 contribution of deforestation, savanna, forest, agricultural, and peat fires (1997-2009),
612 *Atmospheric Chemistry and Physics*, 10(23), 11707-11735, doi: 10.5194/acp-10-11707-2010.

613 Yokota, T., Y. Yoshida, N. Eguchi, Y. Ota, T. Tanaka, H. Watanabe, and S. Maksyutov (2009),
614 Global Concentrations of CO₂ and CH₄ Retrieved from GOSAT: First Preliminary Results
615 *SOLA*, 5, 160-163, doi:10.2151/sola.2009-041.



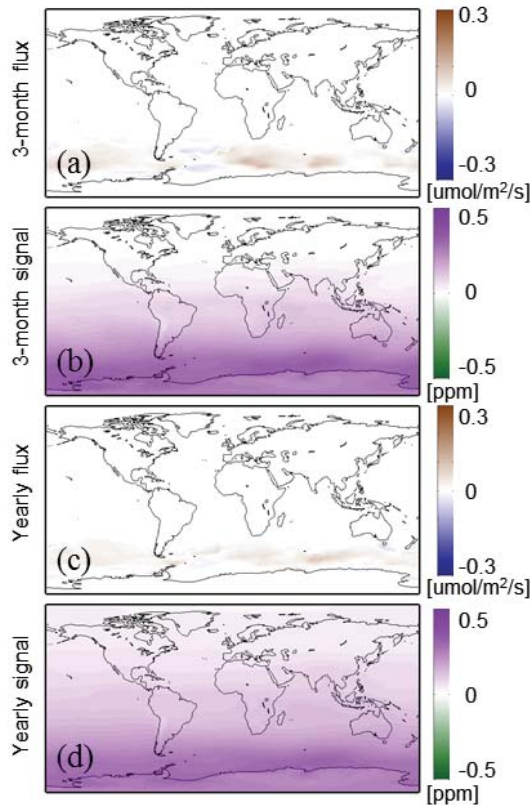
617

618 Figure 1: Flux and CO₂ concentration for the permafrost carbon release experiment. (a) 3-
 619 month average CO₂ flux (“3-month flux”), (b) 3-month average CO₂ concentration (“3-month
 620 signal”), (c) yearly average CO₂ flux (“Yearly flux”), and (d) yearly average CO₂ concentration
 621 (“Yearly signal”). The 3-month period is May through July. The flux is modeled for 2022. The
 622 negative concentration values in the Southern hemisphere are a result of the global mean
 623 adjustment.



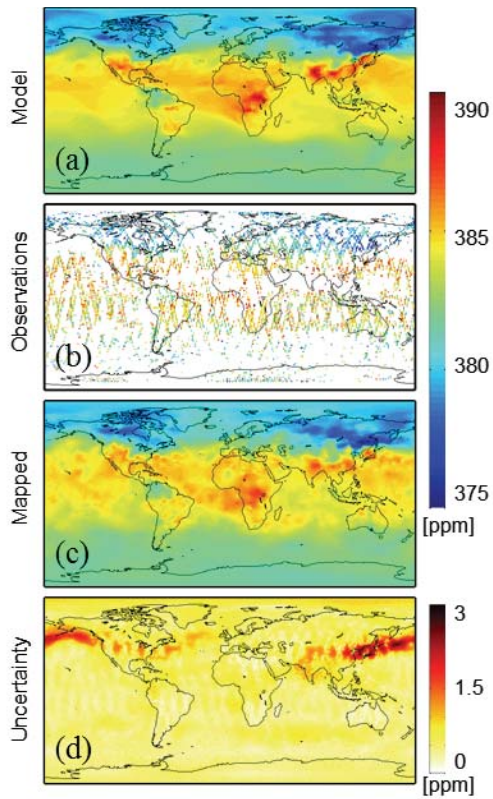
624

625 Figure 2: Flux and CO₂ concentration for the fossil fuel experiments. First row: 3-month
 626 average CO₂ flux (“3-month flux”). Second row: 3-month average CO₂ concentration (“3-month
 627 signal”). Third row: Yearly average CO₂ flux (“Yearly flux”). Fourth row: Yearly average CO₂
 628 concentration (“Yearly signal”). The 3-month period is August through September.



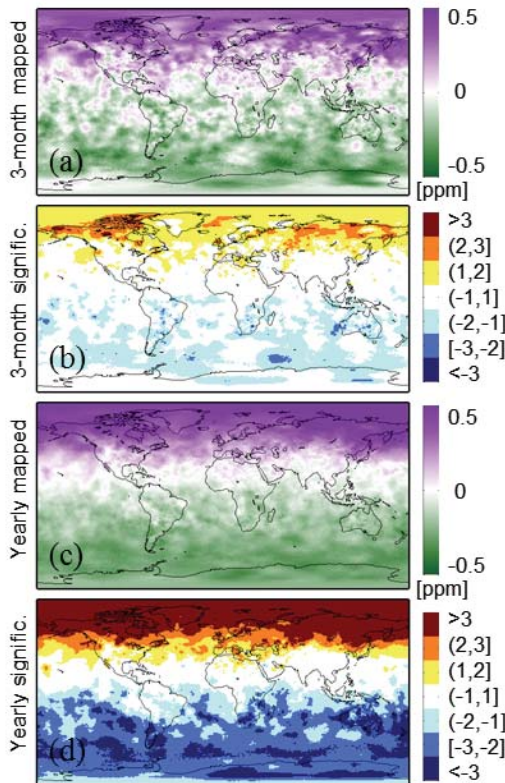
629

630 Figure 3: Flux and CO₂ concentration for the Southern Ocean experiment. (a) 3-month
 631 average CO₂ flux (“3-month flux”), (b) 3-month average CO₂ concentration (“3-month signal”),
 632 (c) yearly average CO₂ flux (“Yearly flux”) and (d) yearly average CO₂ concentration (“Yearly
 633 signal”). The 3-month period is April through June.



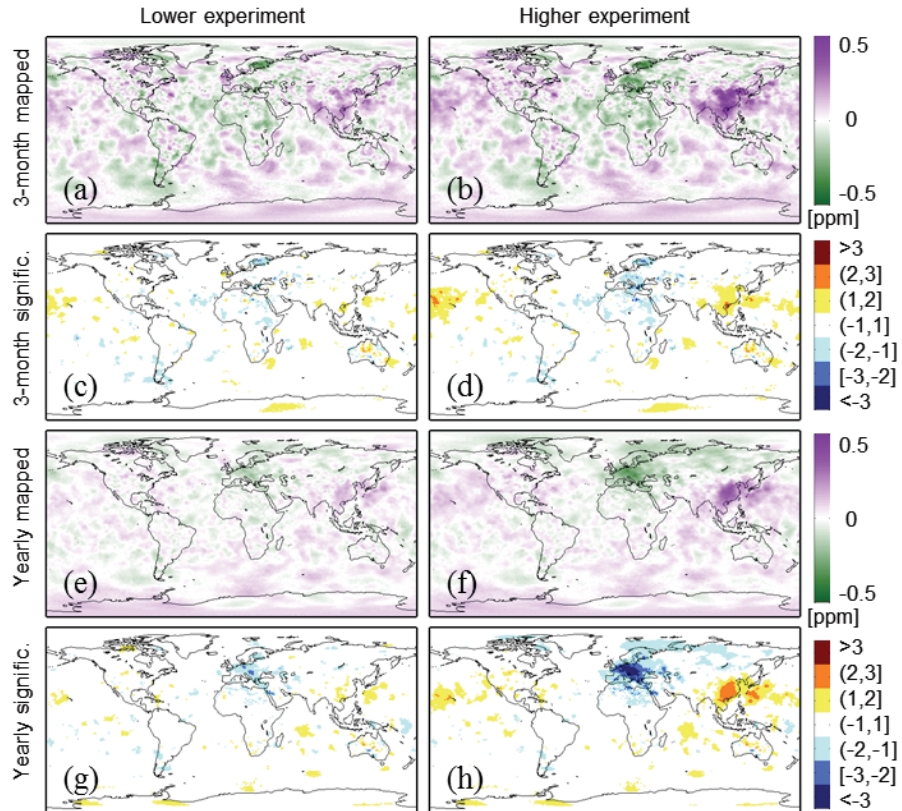
634

635 Figure 4: Mapping results for August 1-4 2007. (a) Modeled CO₂ concentrations (“Model”),
 636 (b) simulated ASCENDS observations (“Observations”), (c) mapped CO₂ concentrations
 637 (“Mapped”), and (d) mapping uncertainties (“Uncertainty”) expressed as a standard deviation.



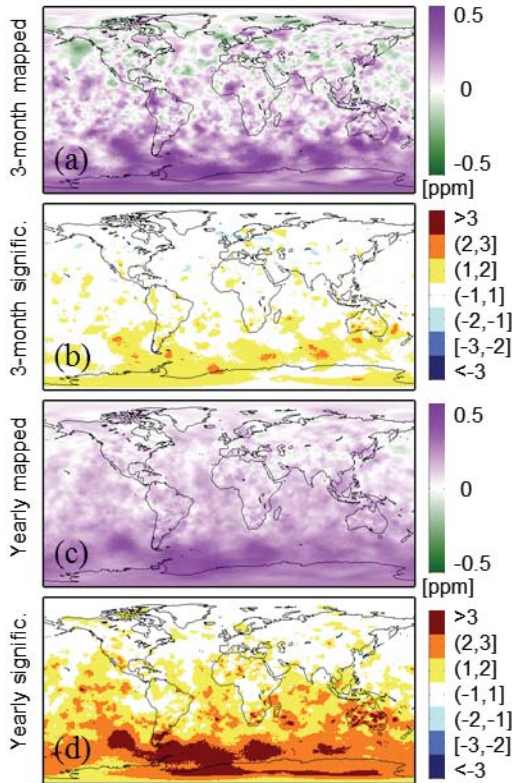
638

639 Figure 5: Results for the permafrost carbon release experiment for medium measurement
 640 noise. (a) 3-month mapped CO₂ signal (“3-month mapped”), (b) Significance of the 3-month
 641 mapped CO₂ signal (“3-month signific.”), (c) Yearly mapped CO₂ signal (“Yearly mapped”), and
 642 (d) Significance of the yearly mapped CO₂ signal (“Yearly signific.”). The mapped signal is the
 643 difference between the mapped perturbation CO₂ concentration and the mapped baseline CO₂
 644 concentration. The significance is the mapped signal divided by the uncertainty of the mapped
 645 signal. The values are discretized for improved visualization. Yellow, orange and dark red
 646 (light, medium and dark blue) represent areas where the mapped perturbation concentration is
 647 larger (smaller) than the mapped baseline concentration by more than one, two or three standard
 648 deviations, respectively, of the uncertainty of the mapped signal. The 3-month period is May
 649 through July.



650

651 Figure 6: Results for the fossil fuel experiments for medium measurement noise. First row:
 652 3-month mapped CO₂ signal (“3-month mapped”). Second row: Significance of the 3-month
 653 mapped CO₂ signal (“3-month signific.”). Third row: Yearly mapped CO₂ signal (“Yearly
 654 mapped”). Fourth row: Significance of the yearly mapped CO₂ signal (“Yearly signific.”). The
 655 mapped signal is the difference between the mapped perturbation CO₂ concentration and the
 656 mapped baseline CO₂ concentration. The significance is the mapped signal divided by the
 657 uncertainty of the mapped signal. The values are discretized for improved visualization.
 658 Yellow, orange and dark red (light, medium and dark blue) represent areas where the mapped
 659 perturbation concentration is larger (smaller) than the mapped baseline concentration by more
 660 than one, two or three standard deviations, respectively, of the uncertainty of the mapped signal.
 661 The 3-month period is August through September.



662

663 Figure 7: Results for the Southern Ocean experiment for medium measurement noise. (a) 3-
 664 month mapped CO₂ signal (“3-month mapped”), (b) Significance of the 3-month mapped CO₂
 665 signal (“3-month signific.”), (c) Yearly mapped CO₂ signal (“Yearly mapped”), and (d)
 666 Significance of the yearly mapped CO₂ signal (“Yearly signific.”). The mapped signal is the
 667 difference between the mapped perturbation CO₂ concentration and the mapped baseline CO₂
 668 concentration. The significance is the mapped signal divided by the uncertainty of the mapped
 669 signal. The values are discretized for improved visualization. Yellow, orange and dark red
 670 (light, medium and dark blue) represent areas where the mapped perturbation concentration is
 671 larger (smaller) than the mapped baseline concentration by more than one, two or three standard
 672 deviations, respectively, of the uncertainty of the mapped signal. The 3-month period is April
 673 through June.